



Fabrication and characterization of well-dispersed plasmonic Pt nanoparticles on Ga-doped ZnO nanopagodas array with enhanced photocatalytic activity



Hsien-Ming Chiu, Tung-Han Yang, Yang-Chih Hsueh, Tsong-Pyng Perng, Jenn-Ming Wu*

Department of Materials Science and Engineering, National Tsing Hua University, 101, sec. 2, Kuang-Fu Road, Hsinchu 30013, Taiwan

ARTICLE INFO

Article history:

Received 30 December 2013
Received in revised form 24 June 2014
Accepted 21 July 2014
Available online 7 August 2014

Keywords:

MOCVD
ZnO
Nanocomposite
Plasmonic
Photocatalysis

ABSTRACT

Pt/GZO hybrid nanocomposites were formed by depositing Pt nanoparticles (NPs) using an atomic layer deposition (ALD) technique onto one-dimensional (1D) Ga-doped ZnO (GZO) nanopagodas (NPGs). The GZO NPGs were prepared by metal–organic chemical vapor deposition (MOCVD). The ALD deposited Pt NPs were well-dispersed and uniform on the surfaces of the GZO NPGs, which were much better than Pt NPs prepared by conventional wet chemistry methods. Pt/GZO hybrid nanocomposites with 30 ALD cycles exhibited significant improvement in photocatalytic activity by about 2.7 times higher than GZO NPGs under 254 nm UV illuminations. The effect of Pt NPs on photocatalytic activities of Pt/GZO hybrid nanocomposites was discussed using various photocatalytic mechanisms. Due to the competing effects of decorated Pt NPs on absorbance/transmittance, electron–hole separation/recombination, and the local surface plasmon resonance, there exists an optimal Pt NPs loading content, which exhibits a maximal photocatalytic activity of 1D Pt/GZO hybrid nanocomposites.

© 2014 Elsevier B.V. All rights reserved.

1. Introduction

Zinc oxide (ZnO), II–VI n-type semiconductor with a direct energy gap of 3.37 eV and a large exciton binding energy of 60 meV [1], is a good candidate material to substitute silicon in pursuit of the next generation electronic and photonic devices. Efforts have been made to develop ZnO nanostructures for various applications such as light-emitting diodes [2,3], laser diodes [1,4], solar cells [5], field emitter [6], field effect transistors [7,8], photodetectors [9,10], and photocatalysis [9]. Among them, photocatalysis of hazardous pollutants have attracted global interests due to the environmental purification and solar energy transformation issue.

In addition to the remarkable progress of TiO₂-based photocatalysts [11–14], pure and doped ZnO-based photocatalysts have also been widely explored [9,15–17]. However, the photocatalytic efficiency of ZnO is always affected by the quick recombination rate of the photogenerated electrons and holes [18,19]. The suppression of electron–hole recombination and the enhancement of electron–hole separation can improve the photocatalytic efficiency. Incorporating noble metal with ZnO is a feasible design for improving the photocatalysis performance. Since the work function of the

noble metal is greater than that of the ZnO, photogenerated electrons in ZnO transfer to and accumulate on the noble metal; while holes remain on the ZnO surface [18–20]. The Schottky barrier, which is formed at the junction, also facilitates the electron capture [21].

Nowadays, most photocatalysts to degrade organic pollutants for wastewater treatment are in nanopowders form. Filtration and/or centrifugation of nanopowders are needed to remove these particulates after waste water treatment [22]. Further, comparing with zero-dimensional (0D) nanoparticles (NPs) and two-dimensional (2D) film-structured, one-dimensional (1D) nanostructures such as wires, rods, tubes, rings, belts, needles, and pagodas are preferable materials for photocatalysis due to their unique properties such as efficient charge transport and large surface area. We had demonstrated that 1D gallium-doped ZnO (GZO) nanopagodas (NPGs) exhibited much better photocatalytic activity than either 2D GZO film or 1D ZnO nanowires (NWs) in one of our previous work [9]. To pursue better performance of photocatalysts, 1D noble metal/ZnO-based hybrid nanocomposites fabricated on solid substrates may be the more feasible structure which is distinct from the traditional method.

Recently, much progress has been made in noble metal/ZnO hybrid nanocomposites. The most studied noble metal/ZnO hybrid nanocomposites are Au and Ag [16,21,23–26], whereas there are few studies on Pd and Pt [19–21,27,28]. Typically, the reported

* Corresponding author. Tel.: +88 635162227.
E-mail address: wu408410@yahoo.com.tw (J.-M. Wu).

Pt/ZnO hybrid nanocomposites photocatalyst are in traditional nanopowders form. The Pt NPs were usually deposited on the support material by chemical reduction of Pt-containing salts in aqueous solution. The drawbacks are particles aggregation, poor durability, and recycle ability. In addition, it is hard to control the size and distribution of Pt NPs, which affect the activity of the catalyst significantly [29–31]. Atomic layer deposition (ALD) is a dry process which exhibits advantages such as good uniformity, precise size control and large-area production for the deposition of Pt catalysts [32].

In this study, we demonstrated a new photocatalysts by depositing 0D Pt NPs via ALD process on 1D GZO NPGs which were synthesized by metal-organic chemical vapor deposition (MOCVD) to form hybrid nanocomposites photocatalyst array on silicon substrates. It exhibits faster and better photodegradation performance. Additionally, they are convenient and easily recyclable as compared with traditional nanopowders and wet solution method. We also discussed the effect of Pt NPs on photocatalytic activities of Pt/GZO hybrid nanocomposites involving photocatalytic mechanisms.

2. Experimental

2.1. Deposition of GZO seed layer:

The GZO seed layer was deposited on Si (100) substrates by radio frequency (RF) magnetron sputtering at room temperature using a 1% GZO target. Before loading into the chamber, the silicon substrates were cut to 2 cm × 2 cm sized samples which were cleaned in ethanol and deionized (DI) water for 30 min by sonication. The samples were then etched by dilute hydrogen fluoride (HF) solution for 2 min to remove the native oxide. Finally, the samples were then rinsed with DI water and purge dried with nitrogen gas (N₂) (99.99%). The sputtering conditions were power 45 W, working pressure 10 mTorr, sputtering gas 100% Ar, and deposition time 1 h. The seed layer was 200 nm thick with a wurtzite (0002) preferred orientation determined by SEM and XRD. The Hall properties of the GZO seed layer were measured. Its carrier concentration was $3.78 \times 10^{19}/\text{cm}^3$, mobility 108.79 cm²/Vs, and resistivity $9.17 \times 10^{-4} \Omega\text{-cm}$. The electrical properties of the GZO seed layer are excellent to serve as back electrodes for further optoelectronic devices measurements and applications.

2.2. Growth of GZO NPGs and ZnO NWs

GZO NPGs were fabricated on the pre-deposited GZO seed layer by metal-organic chemical vapor deposition (MOCVD) technique. Zinc acetylacetonate hydrate [Zn(acac)₂ · xH₂O] (Aldrich, powder), oxygen gas (99.999%), and gallium acetylacetonate [Ga(acac)₃] (Aldrich, 99.99%) were used as the Zn, O, and Ga sources. Nitrogen was introduced as the precursor carrier gas. Zn(acac)₂ · xH₂O and Ga(acac)₃ powders were placed together in an outer glass vessel. The fabrication process was carried out in a horizontal quartz furnace at 750 °C; the outer precursor vessel was heated at 135 °C. The O₂ and N₂ flow rates were kept at 300 and 500 sccm, respectively; the working pressure was maintained at 3–4 Torr by a mechanical pump; and the reaction time was 1 h. The Ga/Zn precursor molar ratios were kept at 0.360 for all GZO NPGs. The Ga content was determined to be about 5.4% by XPS. Pure ZnO NWs without Ga doping were also prepared by the same procedure.

2.3. Decoration of Pt NPs

Pt NPs were synthesized and decorated onto GZO NPGs surfaces by atomic layer deposition (ALD) method. A stainless steel bottle containing (methylcyclopentadienyl)trimethylplatinum (MeCpPtMe₃) as the Pt precursor was interfaced with the pulsing

valve system, the temperature of which was maintained at 45 °C by a temperature controller. O₂ (99.999%) was used as a co-reactant. The substrate heating plate in the chamber was maintained at 280 °C. The ALD cycling number was varied to obtain different amount of Pt NPs. Each ALD cycle consisted of four consecutive steps: a MeCpPtMe₃ pulse, followed by a N₂ purge, and then an O₂ pulse, followed by another N₂ purge.

2.4. Characterization of Pt/GZO hybrid nanocomposites

The surface morphologies and crystal phases of the as-grown nanostructures were examined by field emission scanning electron microscope (FESEM) equipped with an Oxford Instruments INCA energy dispersive X-ray spectroscopy (EDS) system (JEOL, JSM-6500) under an accelerating voltage of 15 kV and by grazing incident X-ray diffraction (GIXRD) technique with a CuKα radiation (PANalytical, X'Pert Pro MRD), respectively. The chemical compositions and binding states of Pt/GZO hybrid nanocomposites were investigated by X-ray photoelectron spectroscopy (XPS) (PHI, PHI-1600). The crystal structures of Pt/GZO hybrid nanocomposites were observed by analytical transmission electron microscope (AEM) (JEOL, JEM-2010) and spherical-aberration corrected field emission atomic resolution analytical electron microscope (Cs-corrected FE-STEM) (JEOL, JEM-ARM200F) under an accelerating voltage of 200 kV. Low-temperature photoluminescence (PL) measurements were carried out using the 325 nm line excitation from a He-Cd laser under 10 K with a cyclic liquid He cooling system (HORIBA, iHR550).

2.5. Photocatalytic activities of Pt/GZO hybrid nanocomposites

UV photocatalytic activity of pristine GZO NPGs and Pt/GZO hybrid nanocomposites with different ALD cycles was evaluated by a representative Rhodamine B (RhB). For each condition, the GZO-based catalysts was immersed into a 2 ppm RhB solution with magnetically stirring in the dark for 30 min to ensure adsorption/desorption equilibrium of RhB with the catalyst. The whole photocatalytic reaction was carried out under 254 nm and 365 nm UV lamp illuminated at room temperature. Each sample was acquired from RhB solution at regular intervals of 20 min to monitor the reaction, and the UV–vis absorption spectra were measured by a UV/vis Spectrometer (PerkinElmer, Lambda 35).

3. Results and discussion

3.1. Characterization of Pt/GZO hybrid nanocomposites

The morphologies of Pt NPs on GZO NPGs with Pt NPs prepared by various ALD cycles were analyzed with SEM and TEM. Fig. 1 shows the SEM images of the tilt-view and the top-view (insets) as well as their corresponding TEM images (Fig. 2) of the representative pristine ZnO NWs, GZO NPGs and Pt/GZO hybrid nanocomposites with various ALD cycles. Fig. 1(a) and Fig. 2(a) show that the pristine ZnO NWs have smooth lateral surfaces. Whereas, Fig. 1(b) and Fig. 2(b) exhibit that pristine GZO NPGs are vertically-aligned with corrugated lateral surfaces similar to a pagoda-shape as reported [6]. Fig. 1(c–h) and Fig. 2(c–h) show morphologies of Pt/GZO hybrid nanocomposites under various ALD cycles. When the cycles of ALD are equal to 10, the decorated Pt NPs are too tiny and too little to be observed by SEM (Fig. 1(c)); however, they can be distinguished by TEM as shown by arrows in Fig. 2(c). When the ALD cycles increase to 30, the decorated Pt NPs can be observed by SEM as indicated by arrows in Fig. 1(d). The corresponding TEM image (Fig. 2(d)) illustrates that well-dispersed Pt NPs are decorated on the GZO NPGs surfaces. With a further increase of the ALD cycling number to 50 and 100, the amounts

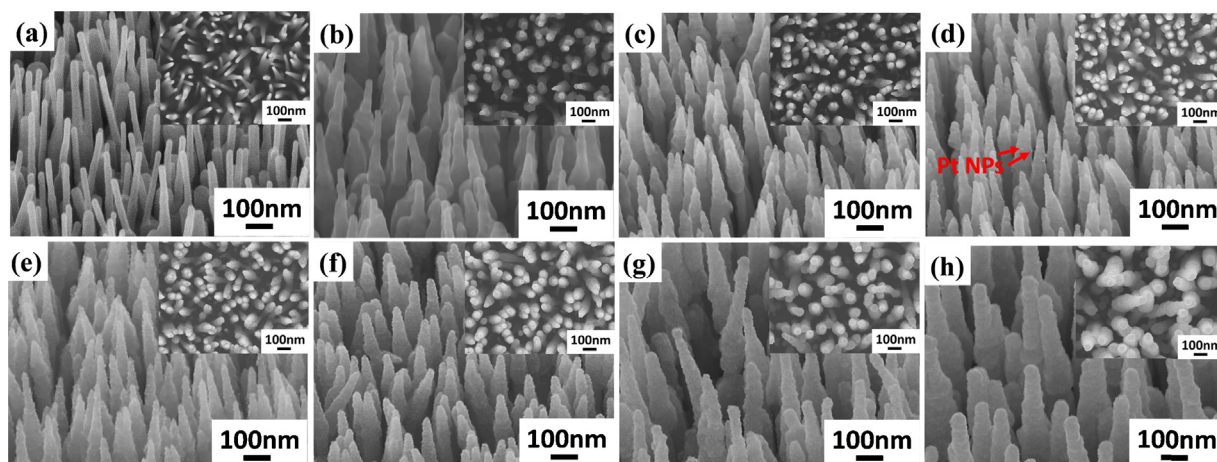


Fig. 1. Tilt-angle SEM images of (a) pristine ZnO NWs; (b) pristine GZO NPGs as well as Pt/GZO hybrid nanocomposites with (c) 10, (d) 30, (e) 50, (f) 100, (g) 150, and (h) 300 ALD cycles. The top-view images are shown in the corresponding insets.

and the diameters of the decorated Pt NPs increase continuously as shown in Fig. 1(e–f) and Fig. 2(e–f). Even under such high amounts, the decorated Pt NPs are still uniformly well-dispersed on the entire GZO NPGs surfaces as revealed from the TEM images. The result demonstrates that the ALD process is very successful in fabricating Pt NPs on GZO NPGs, much better than those prepared by chemical reduction of Pt-containing salts in aqueous solution.

We counted the diameters of Pt NPs directly from the TEM images and depicted the relationship as a function of the number of ALD cycles in Fig. 3(a). The results are summarized in Table 1. The average diameters of decorated Pt NPs slightly increased from 1.8 ± 0.8 to 5.8 ± 1.3 nm when the cycles of ALD increased from 10 to 100.

When the ALD cycles were further increased to 150, the decorated Pt NPs started to aggregate like a film-structure on GZO NPGs surfaces as shown in Fig. 1(g) and Fig. 2(g). Fig. 1(h) and Fig. 2(h) show that the densely decorated Pt NPs aggregate to form a continuous film, i.e. becoming GZO core/Pt shell nanostructures when the cycles of ALD are equal to 300.

Fig. 3(b) shows the Pt 4f core-level XPS signal obtained from the representative Pt/GZO hybrid nanocomposites with 50 ALD cycles.

The Pt NPs loading content determined by XPS range from 0.3 to 7.2% for Pt/GZO hybrid nanocomposites with 10–150 ALD cycles as shown in Fig. 3(a) and listed in Table 1. Further, the peaks locate at 73.8 eV for Pt 4f_{5/2} and 70.5 eV for Pt 4f_{7/2} by using the Gaussian fitting. The peak positions possess lower binding energy than that reported for bulk metallic Pt, 74.7 eV for Pt 4f_{5/2} and 71.5 eV for Pt 4f_{7/2}, respectively [33]. It indicates that there are interactions between the Pt NPs and GZO NPGs [34,35]. Moreover, it is also suggested that the transfer of negative charge from the GZO NPGs to Pt NPs is more likely to occur, causing the shifting of the Pt 4f doublet peak to lower binding energy. Fig. 3(c) shows a core-level Ga 2p_{3/2} peak at 1117.8 eV for the GZO NPGs but none for the ZnO NWs. It demonstrated that Ga atom had doped into ZnO successfully as in our previous report [6,9].

GIXRD was employed to characterize the crystal structures of the top 1D hybrid nanocomposites rather than the bottom seed layer and substrate. Fig. 3(d) shows the GIXRD patterns carried out under a 0.5° grazing angle for GZO NPGs and Pt/GZO hybrid nanocomposites with different ALD cycles (10–300 ALD cycles, which are denoted as G-Pt-10 to G-Pt-300). The pristine GZO NPGs exhibit an intensive and sharp ZnO (0002) diffraction peak at

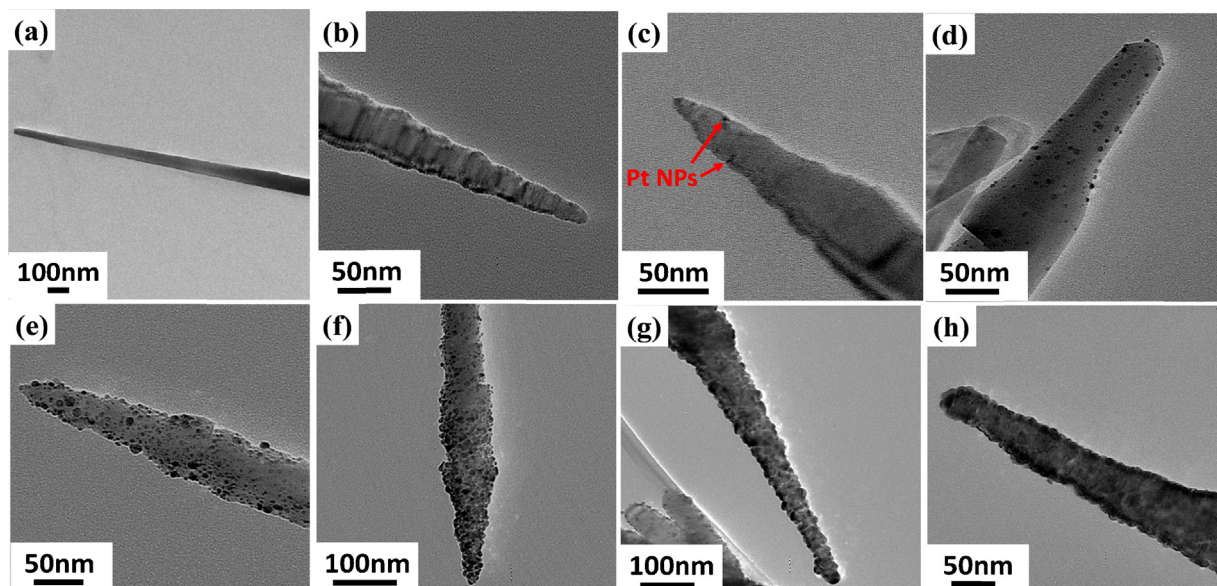


Fig. 2. TEM images of (a) pristine ZnO NWs; (b) pristine GZO NPGs as well as Pt/GZO hybrid nanocomposites with (c) 10, (d) 30, (e) 50, (f) 100, (g) 150, and (h) 300 ALD cycles.

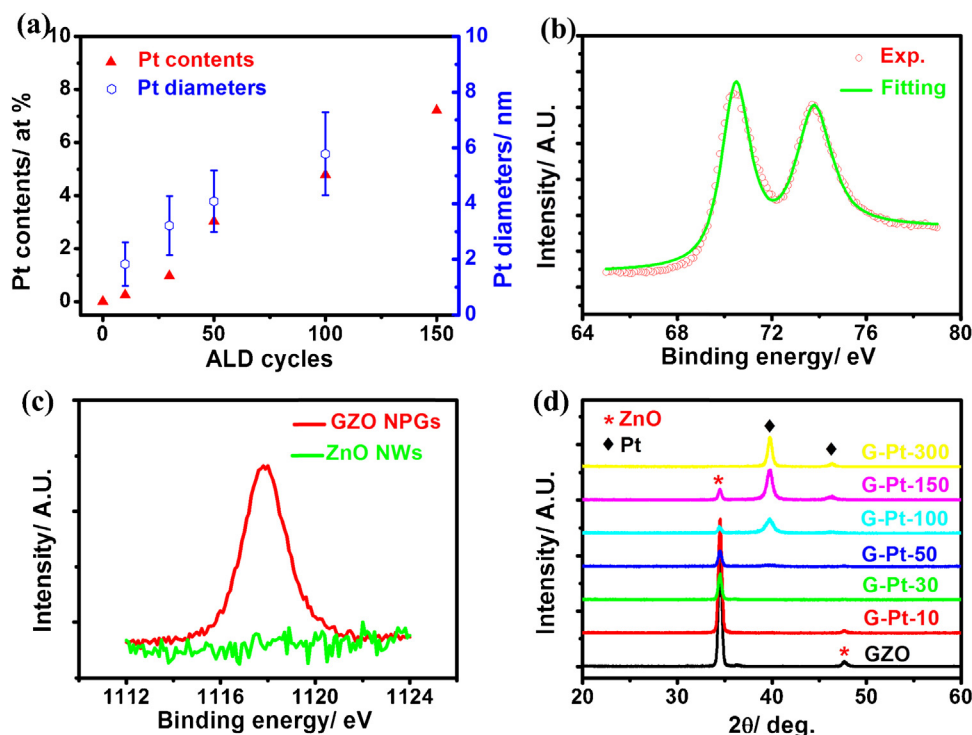


Fig. 3. (a) The content and the diameter of Pt NPs of Pt/GZO hybrid nanocomposites as a function of ALD cycles; (b) the Pt 4f core-level signal obtained from the representative Pt/GZO hybrid nanocomposites with 50 ALD cycles; (c) the Ga 2p_{3/2} core-level signal obtained from the representative GZO NPGs and ZnO NWs; (d) GIXRD patterns of Pt/GZO hybrid nanocomposites with different ALD cycles performed under a 0.5° grazing angle.

ca. 34.52° accompanying with a weak ZnO (1 0 1 2) diffraction peak, i.e. 47.58°. It indicates that the GZO NPGs are essentially vertical to the substrates with only a slight tilt. For Pt/GZO hybrid nanocomposites with 50 and 100 ALD cycles, two diffraction peaks were detected at ca. 39.77° and 46.34°. They were assigned as Pt (1 1 1) and (2 0 0), respectively. It confirms the presence of Pt NPs on GZO NPGs. The decrease of the ZnO peak intensities as well as the increase of the Pt peak intensities with the ALD cycles demonstrate that the loading of Pt NPs on GZO NPGs increases with the ALD cycles. For 300 ALD cycles, the ZnO (0 0 0 2) diffraction peak became vanished with only a prominent Pt (1 1 1) and a weak Pt (2 0 0) diffraction peak. Using goni scan technique, the diffraction peak of ZnO (0 0 0 2) was still prominent as that of Pt (1 1 1) (not shown here).

Fig. 4(a) displays a representative TEM image observed from a single Pt/GZO hybrid nanocomposite with 50 ALD cycles. The inset is a low-magnification image. The contour of a Pt NPs (region B) on the GZO NPG is well-defined. Fig. 4(b) shows the HR-TEM image taken from the region A marked in Fig. 4(a), demonstrating the

excellent crystal quality of the GZO NPG. The lattice spacings of several planes in the HR-TEM image are measured as 0.261, 0.162, and 0.138 nm, which agree well with the values for ZnO (0 0 0 2), (2 1 1 0), and (2 1 1 2) crystal planes, respectively. Crystal planes as well as directions could be deduced by fast Fourier transform (FFT) as a diffraction pattern with a [0 1 1 0] zone axis (inset).

Fig. 4(c) shows the HR-TEM image taken from the region B marked in Fig. 4(a), demonstrating that the decorated Pt NPs exhibit single crystalline. The lattice spacings of several planes in the HR-TEM image are measured as 0.196, 0.225, and 0.139 nm, which are consistent with the values for Pt (0 0 2), (1 1 1), and (2 2 0) crystal planes. Crystal planes as well as directions can be indexed as a diffraction pattern with a [1 1 0] zone axis (inset).

3.2. Photocatalytic activities of Pt/GZO hybrid nanocomposites

To evaluate the photocatalytic activity of the as-prepared Pt/GZO hybrid nanocomposites with different ALD cycles photocatalyst arrays on the RhB photodegradation, we performed

Table 1

Characteristics and photodegradation rate constants (k_a) for RhB under 254 nm UV illumination of Pt/GZO and Pt/ZnO hybrid nanocomposites with different ALD cycles.

Nanostructures	ALD cycles	Pt content [%] ^a	Pt diameters [nm]	k_a (254 nm) [min ⁻¹]	Enhanced ratio ^c	k_a' (365 nm) [min ⁻¹]	R factor [min ⁻¹]
GZO NPGs	0	0	–	0.02324	–	0.02237	0.0087
GZO NPGs	10	0.3	1.8 ± 0.8	–	–	–	–
GZO NPGs	30	1.0	3.2 ± 1.0	0.06376	2.7	0.04142	0.2234
GZO NPGs	50	3.0	4.1 ± 1.1	0.03453	1.5	0.01312	0.2141
GZO NPGs	100	4.8	5.8 ± 1.3	0.01408	0.61	0.00601	0.0807
GZO NPGs	150	7.2	–	0.00958	0.41	0.00460	0.0497
GZO NPGs	300	21.1 ^b	–	0.00509	0.22	0.00311	0.0198
ZnO NWs	0	–	–	0.01473	0.63	–	–
ZnO NWs	30	–	–	0.02266	0.98	–	–
ZnO NWs	100	–	–	0.00955	0.41	–	–

^a Quantification by X-ray photoelectron spectroscopy (XPS).

^b Quantification by energy dispersion spectroscopy (EDS).

^c Use pristine GZO NPGs as the reference.

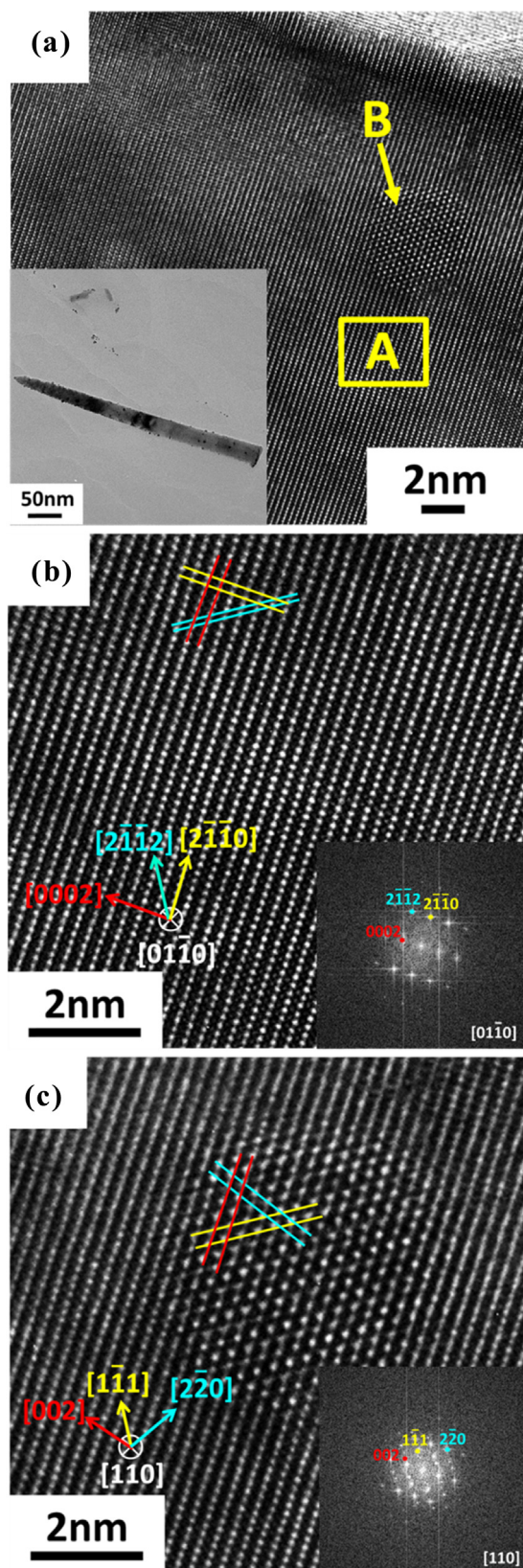


Fig. 4. TEM images of an individual Pt/GZO hybrid nanocomposite with 50 ALD cycles (a) a high-magnification image with a low-magnification one in the inset; (b) a HR-TEM image of GZO NPG (region A in (a)); and (c) a HR-TEM image of Pt NP (region B in (a)); the insets in (b) and (c) are the corresponding FFT diffraction patterns.

the investigation in the presence of 254 nm UV light radiation. Employing RhB as a standard dye, the UV–vis absorption spectra of one representative Pt/GZO hybrid nanocomposites with 30 ALD cycles was illustrated under UV illumination for different irradiation time, as shown in Fig. 5(a). To show absorption curves more clearly, the UV–vis absorption curves of 80, 100, and 120 min were magnified and shown in the left inset. The right insets are the digital photographs which show that the color of the RhB solution turns from pink (0 min) to colorless and clear (120 min). The decrease of the absorption maximum at 554 nm is caused by the deethylation and cleavage of RhB aromatic chromophore ring structure due to the attacking of $\cdot\text{OH}$ and $\cdot\text{O}_2^-$ radicals in the solution. Concurrently, the blue shift of the absorption band is caused by the formation of intermediates in a stepwise deethylation of RhB [12,22].

Fig. 5(b) shows the relative intensity of RhB UV–vis absorption peak as a function of irradiation time, where, C and C_0 are the absorbances of the RhB at irradiation time $t = t$ and 0, respectively, under the wavelength of 554 nm. A RhB solution without any photocatalysts and Pt/GZO hybrid nanocomposites was also tested under the identical condition. The photodegradation rate of the RhB solution without any photocatalysts (self-degradation) was slow. There was about 87% RhB left after 120 min of UV irradiation, the calculated photodegradation rate constant (k_a) was 0.00119 min^{-1} (Fig. 5(c)).

In contrast, the pristine 1D GZO NPGs enhanced the photodegradation rate of RhB (self-degradation) dramatically. We will focus the discussion on the effect of Pt NPs on the photocatalytic activity of the Pt/GZO hybrid nanocomposites first. The photodegradation rate of RhB of Pt/GZO hybrid nanocomposites with ALD cycles less than 30 was enhanced greatly with the loading content of Pt NPs. Nevertheless, that of those Pt/GZO hybrid nanocomposites with ALD cycles higher than 30 started to decrease with the loading content of Pt NPs. When the ALD cycles were higher than 100, the photodegradation rate was slower than the pristine GZO NPGs. The remained RhB after being photodegraded under UV irradiation for 120 min was about 0, 2, 18, 31, and 53% for Pt/GZO hybrid nanocomposites with 30, 50, 100, 150, and 300 ALD cycles, respectively. Nearly 100% photodegradation of the RhB solution was achieved within 120 min under UV irradiation using the Pt/GZO hybrid nanocomposites with ALD cycles less than 50. In addition, this 1D Pt/GZO hybrid nanocomposites (with 30 ALD cycles) possess much faster and better photodegradation performance than reports using traditional nanopowders form [18–21,28].

Since the diameters of decorated Pt NPs do not change significantly with the ALD cycles, the photocatalytic activities depend essentially on the Pt NPs loading content. The results clearly demonstrate that the photocatalytic activities of GZO NPGs are apparently improved by small amount of Pt NPs; however, the photocatalytic activities start to decrease when the Pt NPs loading content exceeds a maximal amount.

The photodegradation of the RhB dye exhibited an exponential decay with time under UV light irradiation. The photodegradation rate can be described by a first-order reaction:

$$\ln\left(\frac{C_0}{C}\right) = k_a t$$

where k_a is the photodegradation rate constant. The $\ln(C_0/C)$ is plotted as a function of the irradiation time in Fig. 5(c). The characteristics of Pt/GZO hybrid nanocomposites carried out with different ALD cycles are summarized in Table 1. The k_a (254 nm) values calculated from the slopes in Fig. 5(c) are 0.02324 min^{-1} for the pristine GZO NPGs, and 0.06376, 0.03453, 0.01408, 0.00958, 0.00509 min^{-1} for Pt/GZO hybrid nanocomposites with 30, 50, 100, 150, 300 ALD cycles, accordingly. It is apparent that the photodegradation rate of Pt/GZO hybrid nanocomposites with 30 ALD cycles was enhanced 2.7-fold faster than that of pristine GZO NPGs.

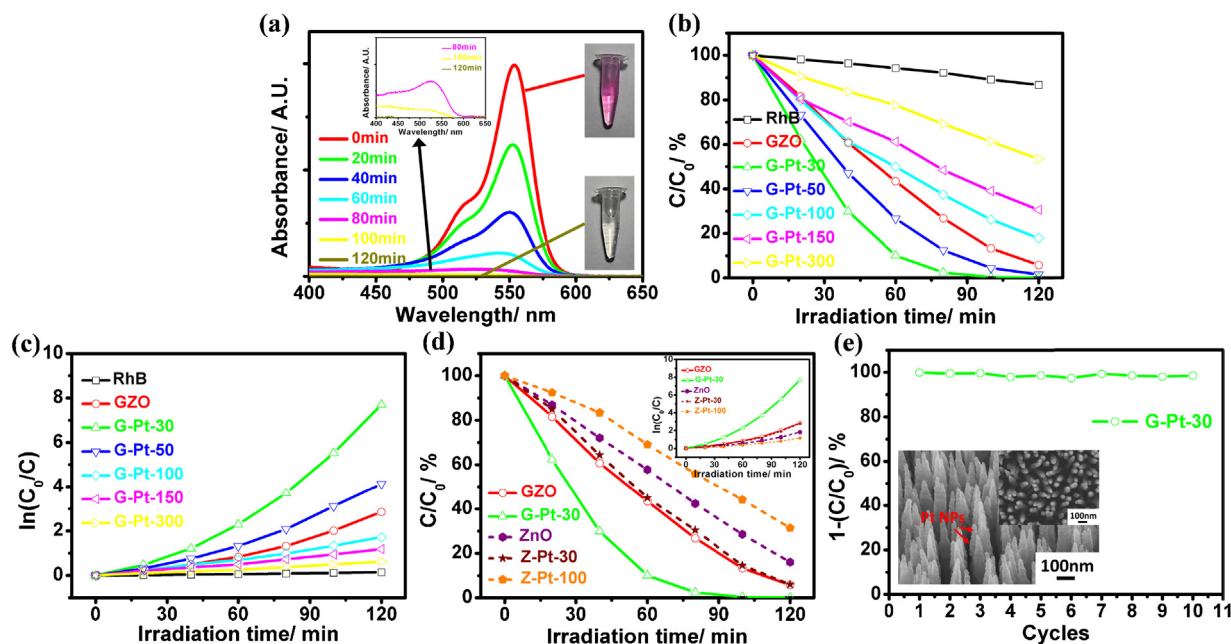


Fig. 5. (a) The time-dependent UV–vis absorption spectra of RhB solution under UV light illumination in the presence of representative a Pt/GZO hybrid nanocomposite with 30 ALD cycles photocatalyst; the left inset is the magnified UV–vis absorption curves of 80, 100, and 120 min taken from (a); the right inset are photographs of colored (initial) and colorless (at 120 min) RhB solutions. Plots of (b) C/C_0 and (c) $\ln(C_0/C)$ of RhB solution as a function of UV light irradiation time for pristine GZO NPGs and Pt/GZO hybrid nanocomposites with different ALD cycles photocatalysts. (d) Plots of C/C_0 and $\ln(C_0/C)$ (inset) of RhB solution as a function of UV light irradiation time for pristine ZnO NWs and Pt/ZnO hybrid nanocomposites with different ALD cycles photocatalysts. (e) Ten cyclic photodegradation of RhB using Pt/GZO hybrid nanocomposite with 30 ALD cycles; inset are the SEM images of tilt-view and the top-view of the Pt/GZO hybrid nanocomposites after ten cyclic photodegradation tests.

Furthermore, the plots are reasonably linear, but with some upward curvature, indicating a deviation from the first-order behavior. When a single reaction pathway is involved primarily in the photodegradation reaction, a first-order rate dependence usually occurs. If more than one reaction pathway was involved (as the reaction 6–8 listed in latter discussion), the overall photodegradation rate, and thus the dependence, might deviate from the first order behavior [22,36,37].

To compare the photocatalytic performance of Pt/ZnO with Pt/GZO hybrid nanocomposites, Fig. 5(d) shows the relative intensity of RhB UV–vis absorption peak and the $\ln(C_0/C)$ (inset) as a function of irradiation time of pristine ZnO NWs as well as several Pt/ZnO hybrid nanocomposites under the same test condition as Pt/GZO ones. The remained RhB after being photodegraded under UV irradiation for 120 min was about 6, 16, and 31% for pristine ZnO NWs, Pt/ZnO hybrid nanocomposites with 30 and 100 ALD cycles, respectively. The k_a (254 nm) values calculated from the slopes in the inset of Fig. 5(d) are 0.01413 min^{-1} for the pristine ZnO NWs, and 0.022666 , 0.00955 min^{-1} for Pt/ZnO hybrid nanocomposites with 30, 100 ALD cycles, accordingly. They were also listed in Table 1.

Here, we can conclude: First, the photocatalytic activity trend of Pt/ZnO hybrid nanocomposites is the same as that of Pt/GZO hybrid nanocomposites, i.e. the photodegradation rate of RhB increases initially and then decreases with further increasing loading content of Pt NPs. Second, the Pt/GZO hybrid nanocomposites possess better performances of RhB photocatalytic reaction than the Pt/ZnO hybrid nanocomposites.

These results are quite similar as compared with either 2D GZO film or 1D ZnO NWs in our previous work [9]. The improved photocatalytic activity of GZO NPGs is attributed to the exposure of the $\{11\bar{2}1\}$, $\{11\bar{2}2\}$, $\{2\bar{2}01\}$, and $\{1101\}$ planes instead of those $\{10\bar{1}0\}$ and $\{11\bar{2}0\}$ planes in pure ZnO NWs. Due to the higher surface energies and the presence of Zn^{2+} -terminated polar state, the $\{11\bar{2}1\}$, $\{11\bar{2}2\}$, $\{2\bar{2}01\}$, and

$\{1101\}$ planes exhibited enhanced O_2 and H_2O chemisorption reactivity.

In addition, to test the stability of the Pt/GZO hybrid nanocomposites, Fig. 5(e) shows 10 cycling runs of the photocatalytic reaction with one of the representative Pt/GZO hybrid nanocomposites with 30 ALD cycles presented in RhB solution under identical conditions. After each cycle, the Pt/GZO hybrid nanocomposites were washed and dried thoroughly, and then fresh RhB solution was added. After 10 cycles, the percentages of RhB photodegradation were above 97% after 120 min under the UV irradiation for each photocatalytic cycle. It demonstrated that the photocatalytic activity of the Pt/GZO hybrid nanocomposites remained unchanged during the cycling stability test. The 1D Pt/GZO hybrid nanocomposites are much more convenient and easily recyclable as compared with traditional nanopowders form. The inset in Fig. 5(e) shows SEM images of the tilt-view and the top-view of one representative Pt/GZO hybrid nanocomposites with 50 ALD cycles. The morphology of the Pt/GZO hybrid nanocomposites was unchanged and remained unaggregated after 10 cycles of test.

3.3. Photocatalytic mechanisms of Pt/GZO hybrid nanocomposites

Photocatalytic reactions associated with Pt/GZO hybrid nanocomposites are summarized and discussed below. Fig. 6 depicts the energy band diagram with respect to the vacuum level of an isolated metallic Pt NP adjacent to an isolated n-type semiconductor GZO NPG. The work functions are 5.3 and 5.6 for ZnO and Pt, respectively, according to the previous reports [38,39]. Electrons and holes are generated when ZnO is illuminated by UV (reaction 1). Due to energy band arrangements, the band of GZO becomes curved upward, and an energy difference (Schottky barrier) of 0.3 eV is created at the contact. As a result, the photo-generated electrons in GZO NPGs either migrate to the surfaces and participate in redox reactions which transform absorbed oxygen

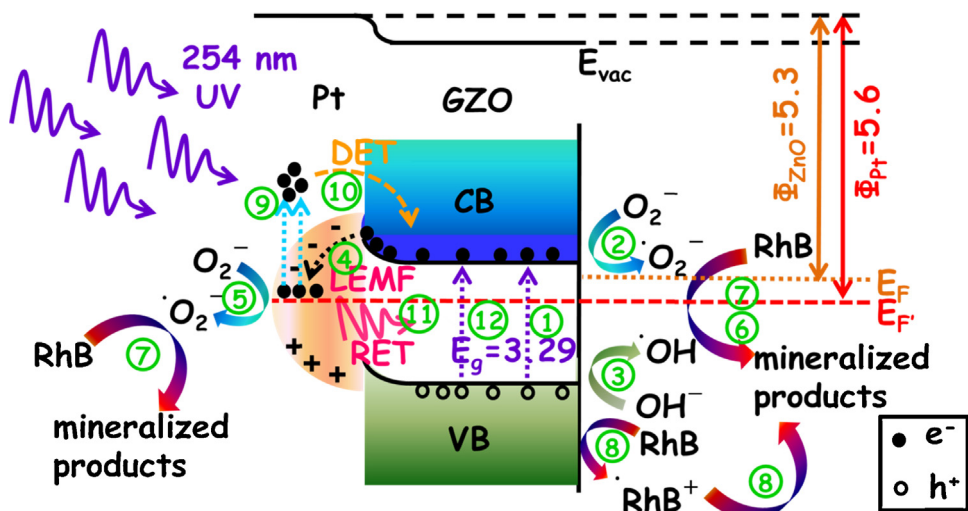
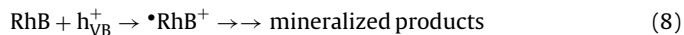
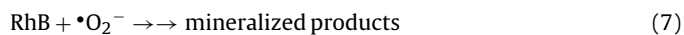
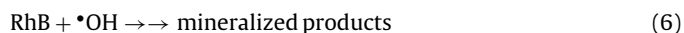
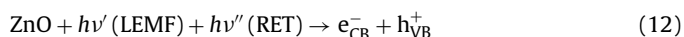


Fig. 6. A schematic diagram contains reactions participating in photocatalysis processes with energy band arrangement of an individual Pt NP/GZO NPG hybrid nanocomposite.

(O_2^-) species to oxygen radicals ($\bullet\text{O}_2^-$) (reaction (2)), or transfer to Pt NPs via tunneling due to the energy difference (reactions (4)) and transform absorbed oxygen (O_2^-) species to oxygen radicals ($\bullet\text{O}_2^-$) (reaction (5)). It is consistent with the observed lower binding energy of the Pt 4f doublet peak signals in the Pt/GZO than the bulk metallic Pt in XPS as shown in Fig. 3(b). Meanwhile, the photogenerated holes in GZO NPGs migrate to the surfaces and participate in redox reactions, transforming the absorbed hydroxyl (OH^-) species to hydroxyl radicals ($\bullet\text{OH}$) due to the depletion layer (reaction (3)). The oxygen $\bullet\text{O}_2^-$ and hydroxyl $\bullet\text{OH}$ radicals, which are extremely strong oxidants, result in the mineralization of organic chemicals (reaction (6–8)). The overall photocatalysis processes can be described by the following reactions:



It is worth noting that the plasmonic Pt NPs can transfer additional photoexcited hot electrons via direct electron transfer (DET) route (reaction (9–10)), and transfer electromagnetic energies by local electromagnetic field enhancement (LEMF) and resonant energy transfer (RET) mechanisms (reaction (11)) into semiconductor GZO NPGs [40]. Eventually, the electromagnetic energies transferred into GZO NPG would further create photogenerated electrons and holes (reaction (12)). These reactions are summarized as followed:



The participative reactions (1–12) which associate with photogenerated electrons and holes as well as gas molecules/radicals

attacking RhB molecules in photocatalysis are also schematically expressed in Fig. 6.

There are several factors affecting the photocatalytic activities of Pt/GZO hybrid nanocomposites according to the listed reactions. They include (i) the optical properties and (ii) the surface plasmonic effects.

3.3.1. Optical properties

As for the optical properties, measurements of UV–vis absorbance/transmittance and PL were performed. The UV–vis absorbance and transmittance spectra of the pristine GZO NPGs and the Pt/GZO hybrid nanocomposites with different ALD cycles were shown in Fig. 7(a) and its inset. Obviously, the pristine GZO NPGs illustrated steep absorption at wavelength shorter than 400 nm, which was attributed to the bandgap of ZnO. In the wavelength range higher than 400 nm, higher absorbance was observed for nanocomposites with higher ALD cycles, i.e. higher Pt NPs loading content. Due to the energy band arrangements, Pt NPs decorated on GZO semiconductors function as electron sinks which enhance the separation of photogenerated electrons and holes (reaction (4)). This effect is increased by the increasing ALD cycles. Consequently, the increase of the ALD cycles enhances the photocatalytic activity (reaction (5)).

In the wavelength region lower than 400 nm, both Pt and GZO absorb light. It is difficult to differentiate the amount of light absorbed by Pt NPs from that absorbed by GZO NPGs. To achieve this, Pt NPs (without GZO) were prepared by the same procedure with different ALD cycles on substrates without the GZO seed layer and NPGs, i.e. the prepared samples contained only Pt NPs on the substrates. Fig. 7(b and c) show the UV–vis transmittance and absorbance spectra of the Pt NPs samples, respectively. Fig. 7(b) illustrates that less light under 400 nm was transmitted by Pt NPs with higher ALD cycles so that less light was absorbed by the underlying GZO NPGs. The light transmitted by Pt NPs and absorbed by GZO NPGs in the Pt/GZO hybrid nanocomposites with different ALD cycles can be estimated by the transmittance at 400 nm. Therefore, photocatalytic activity of Pt/GZO hybrid nanocomposites resulted by reactions (1–3) decreases with increasing ALD cycles due to the lowering light transmission to GZO NPGs. Since the Pt NPs enhance reactions (4–5) and suppress reactions (1–3), there will be an optimal Pt NPs loading content or ALD cycles which results in a maximal photocatalytic activity for the Pt/GZO hybrid nanocomposites.

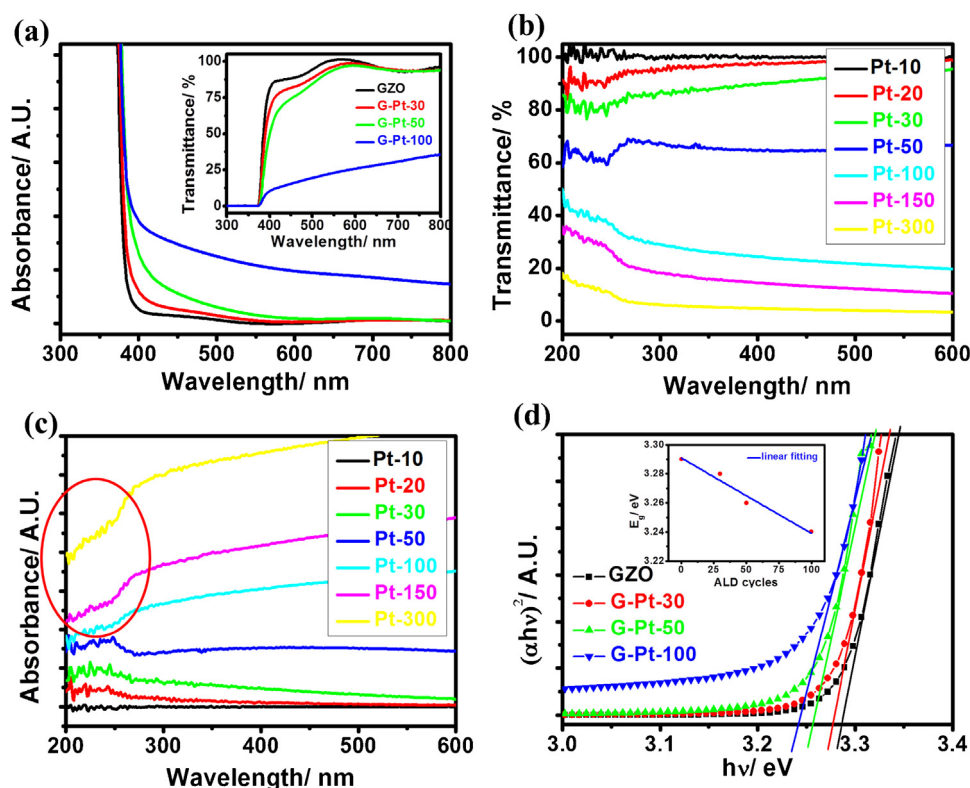


Fig. 7. (a) UV-vis absorbance and transmittance (inset) spectra of pristine GZO NPGs and Pt/GZO hybrid nanocomposites with different ALD cycles; UV-vis (b) transmittance, and (c) absorbance spectra of Pt NPs only with different ALD cycles; (d) plot of $\alpha h\nu$ as a function of the photon energy ($h\nu$) of pristine GZO NPGs and Pt/GZO hybrid nanocomposites with different ALD cycles.

In addition to the amount of light absorbed by the GZO, the amount of photogenerated electrons and holes in the GZO is also affected by the bandgap (E_g) of the GZO, which may be influenced by the Pt NPs. E_g can be estimated using the following equation [41,42]:

$$\alpha h\nu = C(h\nu - E_g)^n \quad (13)$$

where, α is absorption coefficient; $h\nu$ is photon energy; C is a constant; $n = 1/2$ and 2 for a direct and indirect bandgap, respectively. ZnO is a direct bandgap semiconductor. E_g was estimated from the intercepts of the tangents to the $(\alpha h\nu)^2$ versus $h\nu$ plots which are shown in Fig. 7(d) and listed in Table 2. The variation of the E_g of GZO as a function of the number of ALD cycles was depicted in the inset of Fig. 7(d). The bandgap was found to narrow from 3.29 to 3.24 eV with increasing ALD cycling number from 0 to 100. The red-shift of bandgap may be explained by the change of electron concentration in GZO. Zaitsev et al. reported that high density of photoexcited carriers caused a blue-shift in the bandgap of the semiconductor [43]. The electron density in GZO is affected by two effects: first, higher Pt NPs loading content permits more photo-generated electrons transfer from GZO to Pt NPs; second,

higher Pt NPs loading content results in lower transmission of light to generate electron-hole pairs in GZO. Consequently, higher Pt NPs loading contents or higher ALD cycles result in lower electron concentrations in the GZO, which produces a decrease of bandgap or a red-shift. The narrowing of the bandgap promotes the transition of electrons from valence band to conduction band in the GZO, creating more photogenerated electrons and holes (reactions (1) and (12)) and transferring more photogenerated electrons to Pt NPs (reaction (4)).

Photocatalytic reactions also depend strongly on recombination/separation of electron-hole pairs, PL spectra was employed to reveal useful insights. Fig. 8(a) demonstrated the low temperature (10 K) PL spectra of the pristine GZO NPGs as well as the Pt/GZO hybrid nanocomposites with different ALD cycles. All pristine GZO NPGs and Pt/GZO hybrid nanocomposites show only a prominent typical ZnO near-band-edge (NBE) peak near 3.358 eV, which is ascribed to the emission by free excitons, polaritons, and bound excitons, revealing that both pristine GZO NPGs and Pt/GZO hybrid nanocomposites possess excellent crystal qualities. Broad deep-level emission (DL) around 2.5 eV which is usually contributed by defects like oxygen vacancies and zinc interstitials in ZnO are not observed.

The NBE peak is due to the recombination of photogenerated electrons and holes. To examine them more clearly, enlarged NBE peaks are shown in the inset of Fig. 8(a). Noticeably, the NBE peaks show a decrease of intensity and a red-shift of peak position (indicated by dash arrow) with the increase of Pt loading content. The decrease of the NBE intensity depends strongly on the amount of light absorbed by the GZO as well as the suppression of the electron-hole recombination rate by the Pt NPs loading content. The amount of light transmitted by the Pt NPs (at 400 nm) and the relative integrated NBE peak intensity (assume GZO as 100%) are plotted in

Table 2

Characteristics of optical UV-vis transmittance, low-temperature PL spectra, and the fitted optical bandgap energy of Pt/GZO hybrid nanocomposites with different ALD cycles.

ALD cycles	Bandgap [eV]	T%	Center of NBE peak [eV]	PL%
0	3.29	100	3.358	100
30	3.28	90	3.355	75
50	3.26	65	3.353	50
100	3.24	24	–	7

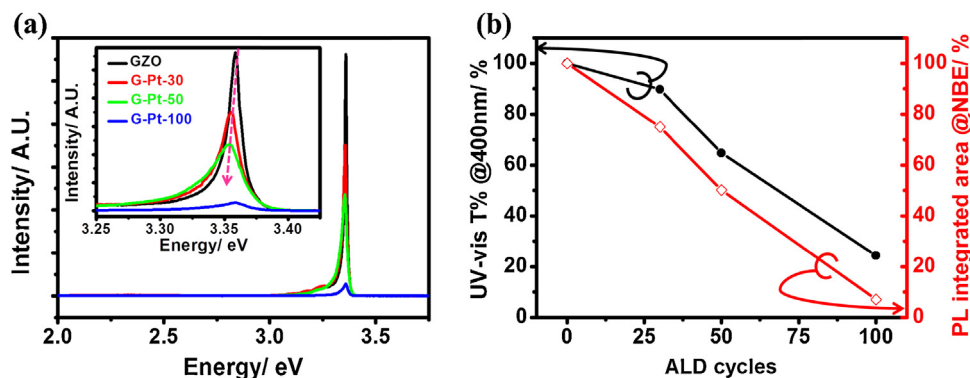


Fig. 8. (a) Low-temperature PL spectra with magnified plots of the near NBE region in the inset of pristine GZO NPGs and Pt/GZO hybrid nanocomposites with different ALD cycles. (b) Transmittance at 400 nm in UV-vis spectra and relative integrated NBE peak area (take GZO as 100%) in PL spectra as a function of ALD cycles.

Fig. 8(b) and listed in Table 2, exhibiting that the PL NBE intensity decreases with the ALD cycles. The two lines are essentially parallel except upon the initial addition of Pt NPs. The decrease trend of the PL NBE intensity with increasing Pt NPs loading content is due to the decrease of light absorbed by the GZO. The decrease of the NBE intensity is larger than the decrease of the light absorbed by GZO upon the initial addition of Pt NPs, indicating that the initial addition of Pt NPs suppresses the recombination rate of electron-hole pairs in GZO. On the other hand, the essential parallelism of lines at further addition of Pt NPs demonstrates that increasing Pt NPs loading content does not improve the recombination rate of electron-hole pairs further.

The red-shift of the NBE peak position suggests the narrowing of the GZO bandgap with increasing Pt NPs loading content, which is consistent with the results in Fig. 7(d). The center of NBE peak is estimated about 3.358, 3.355, and 3.353 eV for Pt/GZO hybrid nanocomposites with 0, 30, and 50 ALD cycles, respectively, which are listed in Table 2. Comparing with the change of E_g estimated by UV-vis spectra, the observed red-shifts by PL are smaller. The full width at half maximum (FWHM) of the NBE peak exhibits a broadening phenomenon, which indicates that the band structure encounters more changes by higher Pt NPs loading content. Bandgap extrapolated from UV-vis measurements may show higher variation due to the band structure change. It may account for the observed differences between the two methods.

3.3.2. Surface plasmonic effect

As for the surface plasmonic effects, Pt NPs can transfer additional photoexcited hot electrons and electromagnetic energies by three routes relating to the plasmonic effect (reaction (9–12)), which consequently improves the photocatalytic activity under UV light irradiation. Fig. 7(c) shows that broad absorbance peak occurs when the wavelength is smaller than 260 nm for Pt NPs with ALD cycles 20, 30, and 50. It is due to local surface plasmon resonance (LSPR). The LSPR was reported to locate at 258 nm for 4.5 nm Pt NPs [44]. In our case, the broad absorbance peak occurs at around 248 nm for the 4.1 nm Pt NPs (with 50 ALD cycles). Due to the quantum confinement effect, the absorbance peak was reported to exhibit a blue-shift when the diameter (size) of particles decreased. It explains the result that the LSPR of the Pt NPs (with 50 ALD cycles) occurs at shorter wavelength than the reported value.

For ALD cycles higher than 100, no LSPR is observed, and the absorbance decreases with the decreasing wavelength (indicated by circle). The diameter and the loading content of the Pt NPs are 5.8 nm and 4.8%, respectively, for Pt/GZO hybrid nanocomposites with 100 ALD cycles. It is ascribed partly to the increasing diameter

of the Pt NPs, which suppress the intensity of the absorbance peak [45], and partly due to the high density of the Pt NPs so that Pt NPs aggregate to form a film-like structure (confirmed by SEM images, not shown here). The maximal photocatalytic activity occurs at Pt/GZO hybrid nanocomposites with 30 ALD cycles which exhibits a strong LSPR effect.

As a consequence, due to the competing effects of decorated Pt NPs on absorbance/transmittance, electron-hole separation/recombination, and the LSPR, there exists an optimal Pt NPs loading content which exhibits a maximal photocatalytic activity of 1D Pt/GZO hybrid nanocomposites. The optimal Pt NPs loading content occurs at 30 ALD cycles for the Pt/GZO hybrid nanocomposites in this study.

Finally, to extract the LSPR effect on the photocatalytic activity, the RhB photocatalytic reaction of Pt/GZO hybrid nanocomposites were also performed under the 365 nm UV light radiation. Fig. 9(a) shows the relative intensity of RhB UV-vis absorption peak (C_0/C) and Fig. 9(b) shows the $\ln(C_0/C)$ as a function of irradiation time of pristine GZO NPGs as well as several Pt/GZO hybrid nanocomposites with various ALD cycles under the same test condition as above except using the 365 nm UV light radiation. The remained RhB after being photodegraded under UV irradiation for 120 min, and the photodegradation rate constant k_a (365 nm) values calculated from the slopes in Fig. 9(b) are about (7%, 0.02237 min⁻¹), (1%, 0.04142 min⁻¹), (21%, 0.01312 min⁻¹), (50%, 0.00601 min⁻¹), (59%, 0.00460 min⁻¹), and (70%, 0.00311 min⁻¹) for pristine GZO, Pt/GZO hybrid nanocomposites with 30, 50, 100, 150 and 300 ALD cycles, accordingly. They were also listed in Table 1.

Moreover, a factor R can be defined to quantify the effect as follows:

$$R = k_a(254 \text{ nm}) - k_a'(365 \text{ nm}) \quad (14)$$

Based on the calculated R , some conclusions can be obtained. First, the $k_a'(365 \text{ nm})$ is smaller than $k_a(254 \text{ nm})$; it is partly due to the contribution of LSPR effect, and partly due to the difference of the competing effects of absorbance/transmittance and electron-hole separation/recombination of decorated Pt NPs under 365 and 254 nm light irradiation. Second, the R factor of GZO NPGs is only 0.0087 min⁻¹, which may be attributed to the effect caused by the energy difference of these two UV light sources. As for Pt/GZO hybrid nanocomposites, the R values are much larger than 0.0087 min⁻¹. Among them, the R values of Pt/GZO hybrid nanocomposites with 30 and 50 ALD cycles are about 25 times of this value. It is considered mainly due to the LSPR effect. The R value decreases with the increasing ALD cycles of Pt NPs. The maximal LSPR effect occurs at Pt/GZO hybrid nanocomposites with 30–50 ALD cycles, which is compatible with the result observed in

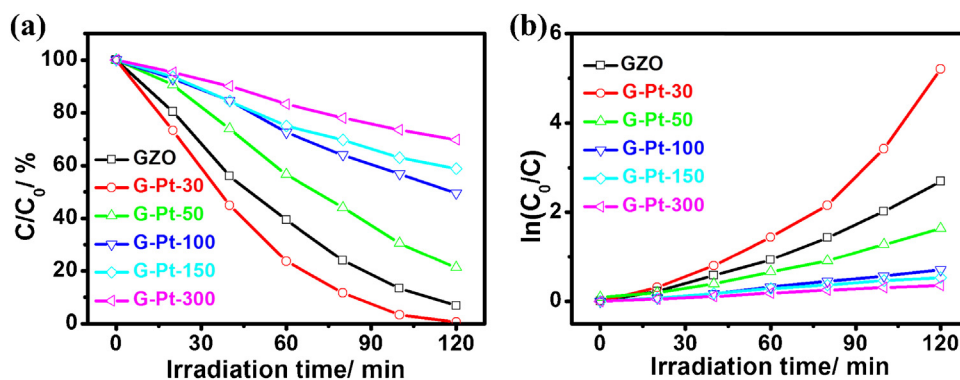


Fig. 9. Plots of (a) C/C_0 and (b) $\ln(C_0/C)$ of RhB solution as a function of irradiation time under 365 nm UV light for pristine GZO NPGs and Pt/GZO hybrid nanocomposites with various ALD cycles.

Fig. 7(c). It is noted that the R values of Pt/GZO hybrid nanocomposites with ALD cycles higher than 100 are about 2~9 times of the value 0.0087 min^{-1} , which is considered mainly due to the overall competing effects of absorbance/transmittance and electron-hole separation/recombination of decorated Pt NPs.

4. Conclusions

1D Pt/GZO hybrid nanocomposites were formed by fabricating the GZO NPGs using MOCVD first, followed by depositing Pt NPs onto GZO NPGs through an ALD technique. Both GZO NPGs and Pt NPs possess excellent crystal qualities as demonstrated by HR-TEM and low temperature PL. Pt/GZO hybrid nanocomposites with 30 ALD cycles exhibited significant improvement in the photocatalytic activity under 254 nm UV illumination by about 2.7 times which are higher than the pristine GZO NPGs. Pt NPs not only serve as electron sinks to effectively separate photogenerated electrons and holes, but also create numerous additional active adsorption sites for photocatalysis. Moreover, Pt NPs act as plasmonic centres, which transferred additional photoexcited hot electrons via DET route as well as electromagnetic energies by LEMF and RET mechanisms into GZO NPGs, forming more photogenerated electrons and holes for catalysis. However, Pt NPs reduce the transmittance of light to GZO, which decrease the photocatalytic activity of GZO. Due to the competing effects of decorated Pt NPs on the absorbance/transmittance, electron-hole separation/recombination, and the LSPR effect, there exists an optimal Pt NPs loading content, which exhibits a maximal photocatalytic activity of 1D Pt/GZO hybrid nanocomposites. The optimal Pt NPs loading content occurs at 30 ALD cycles for the Pt/GZO hybrid nanocomposites in this study. Based on the results of RhB photodegradation reaction of Pt/GZO hybrid nanocomposites with various ALD cycles under 365 nm UV illumination, the LSPR effect of decorated Pt NPs is maximal for Pt/GZO hybrid nanocomposites with 30–50 ALD cycles, it is in accordance with that in 254 nm UV illumination.

Acknowledgements

The authors gratefully acknowledge the National Science Council of the Republic of China for financial support under Contract NSC102-2221-E-007-049-MY3 and appreciate the National Nano Device Laboratories for facilities support.

References

- [1] M.H. Huang, S. Mao, H. Feick, H.Q. Yan, Y.Y. Wu, H. Kind, E. Weber, R. Russo, P.D. Yang, *Science* 292 (2001) 1897–1899.
- [2] M. Willander, O. Nur, N. Bano, K. Sultana, *New J. Phys.* 11 (2009) 125020.
- [3] W.I. Park, G.C. Yi, *Adv. Mater.* 16 (2004) 87–90.
- [4] W.M. Kwok, A.B. Djuricic, Y.H. Leung, W.K. Chan, D.L. Phillips, *Appl. Phys. Lett.* 87 (2005) 093108.
- [5] A.B.F. Martinson, J.W. Elam, J.T. Hupp, M.J. Pellin, *Nano Lett.* 7 (2007) 2183–2187.
- [6] H.-M. Chiu, H.-J. Tsai, W.-K. Hsu, J.-M. Wu, *Crystengcomm* 15 (2013) 5764–5775.
- [7] M.S. Arnold, P. Avouris, Z.W. Pan, Z.L. Wang, *J. Phys. Chem. B* 107 (2003) 659–663.
- [8] G.D. Yuan, W.J. Zhang, J.S. Jie, X. Fan, J.X. Tang, I. Shafiq, Z.Z. Ye, C.S. Lee, S.T. Lee, *Adv. Mater.* 20 (2008) 168–173.
- [9] H.-M. Chiu, J.-M. Wu, *J. Mater. Chem. A* 1 (2013) 5524–5534.
- [10] W.Y. Weng, S.J. Chang, C.L. Hsu, T.J. Hsueh, S.P. Chang, *J. Electrochem. Soc.* 157 (2010) K30–K33.
- [11] X. Wang, T. Dornom, M. Blackford, R.A. Caruso, *J. Mater. Chem.* 22 (2012) 11701–11710.
- [12] Y. Zhao, C. Li, X. Liu, F. Go, H.L. Du, L. Shi, *Appl. Catal. B-Environ.* 79 (2008) 208–215.
- [13] T.J. Athauda, J.G. Neff, L. Sutherlin, U. Butt, R.R. Ozer, *ACS Appl. Mater. Interf.* 4 (2012) 6916–6925.
- [14] R.-H. Tao, J.-M. Wu, J.-Z. Xiao, Y.-P. Zhao, W.-W. Dong, X.-D. Fang, *Appl. Surf. Sci.* 279 (2013) 324–328.
- [15] Z.Z. Han, L. Liao, Y.T. Wu, H.B. Pan, S.F. Shen, J.Z. Chen, *J. Hazard. Mater.* 217 (2012) 100–106.
- [16] D.D. Lin, H. Wu, R. Zhang, W. Pan, *Chem. Mater.* 21 (2009) 3479–3484.
- [17] Y.L. Lai, M. Meng, Y.F. Yu, *Appl. Catal. B-Environ.* 100 (2010) 491–501.
- [18] J. Yuan, E.S.G. Choo, X. Tang, Y. Sheng, J. Ding, J. Xue, *Nanotechnology* 21 (2010) 185606.
- [19] C. Yu, K. Yang, Y. Xie, Q. Fan, J.C. Yu, Q. Shu, C. Wang, *Nanoscale* 5 (2013) 2142–2151.
- [20] J.W. Chiou, S.C. Ray, H.M. Tsai, C.W. Pao, F.Z. Chien, W.F. Pong, C.H. Tseng, J.J. Wu, M.H. Tsai, C.H. Chen, H.J. Lin, J.F. Lee, J.H. Guo, *J. Phys. Chem. C* 115 (2011) 2650–2655.
- [21] P. Pawinrat, O. Mekasuwandumrong, J. Panpranot, *Catal. Commun.* 10 (2009) 1380–1385.
- [22] S. Horikoshi, A. Saitou, H. Hidaka, N. Serpone, *Environ. Sci. Technol.* 37 (2003) 5813–5822.
- [23] P. Li, Z. Wei, T. Wu, Q. Peng, Y. Li, *J. Am. Chem. Soc.* 133 (2011) 5660–5663.
- [24] G. Sinha, L.E. Depero, I. Alessandri, *ACS Appl. Mater. Interf.* 3 (2011) 2557–2563.
- [25] Y. Zheng, L. Zheng, Y. Zhan, X. Lin, Q. Zheng, K. Wei, *Inorg. Chem.* 46 (2007) 6980–6986.
- [26] A.A. Ashkarran, *Appl. Phys. A-Mater. Sci. Process.* 107 (2012) 401–410.
- [27] L.Q. Jing, B.Q. Wang, B.F. Xin, S.D. Li, K.Y. Shi, W.M. Cai, H.G. Fu, *J. Solid State Chem.* 177 (2004) 4221–4227.
- [28] Y. Zhang, J. Xu, P. Xu, Y. Zhu, X. Chen, W. Yu, *Nanotechnology* 21 (2010) 285501.
- [29] F.E. Osterloh, *Chem. Soc. Rev.* 42 (2013) 2294–2320.
- [30] S.C. Warren, E. Thimsen, *Energy Environ. Sci.* 5 (2012) 5133–5146.
- [31] X. Zhang, Y.L. Chen, R.-S. Liu, D.P. Tsai, *Rep. Prog. Phys.* 76 (2013) 046401.
- [32] Y.-C. Hsueh, C.-C. Wang, C. Liu, C.-C. Kei, T.-P. Perng, *Nanotechnology* 23 (2012) 405603.
- [33] J. Despres, M. Elsener, M. Koebel, O. Krocher, B. Schnyder, A. Wokaun, *Appl. Catal. B-Environ.* 50 (2004) 73–82.
- [34] S. Laursen, S. Linic, *Phys. Rev. Lett.* 97 (2006) 026101.
- [35] P. Blumentrit, M. Yoshitake, S. Nemsak, T. Kim, T. Nagata, *Appl. Surf. Sci.* 258 (2011) 780–785.
- [36] S.R. Schmidt, *Catalysis of Organic Reactions: Twenty-first Conference, Florida, CRC Press, Boca Raton, 2006.*
- [37] J.R. Sowa Jr., *Catalysis of Organic Reactions, CRC Press, Boca Raton, Florida, 2005.*

- [38] S.W. Kan, S.K. Mohanta, Y.Y. Kim, H.K. Cho, *Cryst. Growth Des.* 8 (2008) 1458–1460.
- [39] K.D. Schierbaum, S. Fischer, M.C. Torquemada, J.L. deSegovia, E. Roman, J.A. MartinGago, *Surf. Sci.* 345 (1996) 261–273.
- [40] S.K. Cushing, J., Li, F., Meng, T.R., Senty, S., Suri, M., Zhi, M., Li, A.D., Bristow, N., Wu, J. *Am. Chem. Soc.*, 134 (2012) 15033–15041.
- [41] A.M. Salem, M.S. Selim, *J. Phys. D: Appl. Phys.* 34 (2001) 12–17.
- [42] O. Koshy, M.A. Khadar, *J. Appl. Phys.* 109 (2011) 124315.
- [43] S.V. Zaitsev, V.D. Kulakovskii, A.A. Maksimov, D.A. Pronin, I.I. Tartakovskii, N.A. Gippius, M.T. Litz, F. Fisher, A. Waag, D.R. Yakovlev, W. Ossau, G. Landwehr, *JETP Lett.* 66 (1997) 376–381.
- [44] S. Mandal, P.R. Selvakannan, D. Roy, R.V. Chaudhari, M. Sastry, *Chem. Commun.* (2002) 3002–3003.
- [45] B. Khlebtsov, V. Zharov, A. Melnikov, V. Tuchin, N. Khlebtsov, *Nanotechnology* 17 (2006) 5167–5179.